Effect of the Helically-trapped Energetic-ion-driven Resistive Interchange Modes on Energetic Ion Confinement in the Large Helical Device

K. Ogawa[1, 2], M. Isobe[1, 2], H. Kawase[2], T. Nishitani[1], R. Seki[1, 2], M. Osakabe[1, 2], and LHD Experiment Group[1]

1) National Institute for Fusion Science, National Institutes of Natural Sciences, Toki-city, Gifu, Japan
2) SOKENDAI (The Graduate University for Advanced Studies), Toki, Japan

Abstract

The effect of the helically-trapped energetic-ion-driven resistive interchange modes (EICs) on energetic ion confinement is studied in the Large Helical Device (LHD) deuterium plasmas. Neutron diagnostics such as the neutron flux monitor (NFM) and the vertical neutron camera (VNC) are used in order to measure neutrons mainly created by beam-plasma reactions. The line-integrated neutron profiles are obtained by VNC in magnetohydrodynamic-quiet plasma with various neutral beam (NB) injection patterns. The profiles are consistent with that expected by the beam ion density calculated using orbit-following simulations. Significant decreases of the total neutron emission rate (S_n) and the neutron counting rate of the VNC (C_n) in central cords are observed to be synchronized with EIC bursts with perpendicular-NB injection. The drop rates of both S_n and C_n increase with EIC amplitude and reach around 50 %. The line-integrated neutron profiles before and after EIC burst show that in the central cords, C_n decrease due to EIC burst whereas there is almost no change in the other cords. The experimental results suggests that the effect of EIC on helically-trapped beam ion is substantial, however the effect of passing beam ion is not significant.

Keywords: Energetic ion transport, Neutron diagnostics, The Large Helical Device

Introduction

Neutrons are created mainly from beam-plasma reactions in current LHD neutral-beam-heated deuterium (D) plasmas. Neutron diagnostics have been widely used for studying energetic ion physics, especially in large tokamaks [1]. For example, a neutron flux monitor (NFM) consisting of a thermal neutron detector is used for understanding the global confinement of energetic ions, a neutron camera (NC) is used for understanding the radial profile of the energetic ion density, and a neutron energy spectrometer is used

for understanding the velocity distribution of energetic ions [2]. Beam ion transport and loss due to energetic-particle-driven magnetohydrodynamic (MHD) mode has been studied by means of the NFM and the NC in large tokamaks such as TFTR, JET and JT60-U [3-8]. In ITER, radial and vertical NCs are planned for studying spatial profiles of the neutron emission and the alpha-particle birth, the fuel burnup rate, plasma positions, the ion temperature, and the fuel densities [9]. A typical example of energetic particle-driven instability is fishbone which is classified into the energetic particle modes [10] arises from the resonance of trapped beam ions and internal kink mode. Significant drop of neutron emission rate due to fishbone instability indicating that the instability degrades the confinement of the fast ions because neutrons are mainly created due to beam-thermal reactions in these discharges [11-16]. In stellarators and helical devices, energetic ion physics research has been studied in the Large Helical Device (LHD) using intensive neutral beam injections (NBs) [17]. The energetic particle driven MHD mode called the helically-trapped energetic-ion-driven resistive interchange mode (EIC) are often excited by intensive perpendicular NB injections. The resonance between resistive interchange modes having poloidal mode number/toroidal mode number of 1/1 and the precession motion of helically-trapped beam ions causes the EIC [18]. It is reported that the peak position of EIC is located at r/a of around 0.85 and width is less than 0.06 m. Fast-neutral flux measured by the compact neutral analyzer and the change of plasma potential measured by the heavy ion beam probe show that energetic ions might be transported to outer region. The D experiment was initiated from March 2017 [19]. One of the goals is expanding energetic ion physics to understand the effect of the EIC on the beam ion confinement, beam ion transport and/or beam ion loss by means of the comprehensive neutron diagnostics installed on the LHD such as the NFM [20] and the vertical neutron camera (VNC) [21]. Section 2 provides brief introductions of NFM, VNC, and characteristics of beam ion orbits and typical beam ion density in LHD. The measurement of S_n and line-integrated neutron emission profile with and without EIC burst in various NB injection conditions are reported in section 3. The summary is described in section 4.

2. Experimental Setup

Experiments are performed in the LHD, which has a major radius of 3.9 m and averaged minor radius of ~0.6 m. The LHD is equipped with three tangentially-injected negative ion based 180 keV neutral beam injectors (NNB), two perpendicularly-injected positive-ion based 40/80 keV neutral beam injectors (PNB) and a 5.3 MW electron cyclotron heating (ECH) system. The tangency radius of NNB1 and NNB2 are 3.75 m, whereas that of NNB3 is 3.70 m. The typical total injection powers of NNB and PNB are 15 MW and

18 MW, respectively. NNB creates beam ions having the pitch angle of around 30 degrees corresponding to passing ions, whereas PNB creates beam ions having the pitch angle around 90 degrees corresponding to helically trapped ions. The absolutely calibrated primary fission chamber which is the part of NFM installed on the central axis of the LHD is used to measure the total neutron emission rate (S_n). The NFM is characterized by fast response (time resolution of 0.5 ms), wide dynamic range (ten orders of magnitude), and high noise tolerance, which are realized by the digital signal processing unit equipped with a leading edge field programmable gate array (FPGA). The details of NFM are discussed in Ref. 16. The VNC installed on the basement level of the torus hall is used to measure line-integrated neutron profiles (Fig.1) [21]. The VNC consisting of a collimator made from a heavy concrete (3.5 g/cc), stilbene fast-neutron scintillation detectors coupled with a photomultiplier having a high-gain stability with external DC power supplies in order to suppress the gain shift in the high-counting region, and the data acquisition system (DAQ) equipped with 14 bits 1 GHz sampling analogue to digital converter and FPGA. The DAQ is characterized by the wide dynamic range; it can stably operate over MHz counting rate region. The waveform acquired with 1 GHz sampling rate and shaping parameters of each pulse can be stored simultaneously. Therefore, online and offline neutron-gamma discrimination are possible. In this experiment, offline neutron-gamma discrimination is performed to extract the pulse induced by the neutron. The radiation power (P_{rad}) is measured by the resistive bolometer [22], the central electron temperature (T_{e0}) is measured by the Thomson scattering diagnostics [23], and the magnetic fluctuation amplitude (b_θ) is measured by the Mirnov coil installed on the vacuum vessel [24].

Figure 2 shows typical guiding center beam ion orbits of (a) co-going and (b) helically-trapped ions with the LHD plasma. Here the orbit is calculated by using the five dimensional orbit following code DELTA5D [25] with the equilibrium reconstructed by VMEC2000 [26]. Here, energy/pitch angle of co-going ion is set to be typical value of NNB ion 180 keV/25 degrees and that of helically trapped ion is set to be typical value of PNB ion 80 keV/85 degrees. The color denotes the magnetic field strength. The magnetic field on both sides of the vertical elongated cross section is stronger because of the helical coils. The orbit of the passing particle is similar to the orbit of passing particle in Tokamaks. The helically-trapped-ion-orbit shows that the ion is trapped in the helical ripple and can move around the torus along the valley of magnetic field. Figure 3 shows typical density profile of beam ion injected by NNB [27] and PNB [28] evaluated with the MORH code [29] in the vertical elongated cross section where the VNC installed. The MORH code is based on orbit following models with considering slowing down of beam

ions in real coordinates with the Monte Carlo method. Here, initial energies of NNB-injected ions are 180 keV and those of PNB injected ions are 80 keV. In this calculation the birth profile of beam ion is calculated by the HFREYA code which is part of the FIT3D code [30]. As expected by the single orbit calculation shown in Fig.2, the density profile of the passing ions is nearly symmetrical with the poloidal angle, whereas the density profile of the helically-trapped ions has the poloidal structure. The helically-trapped ions are accumulated in the magnetic field valley.

3. Experimental Results

Line-integrated neutron profiles are measured in D plasmas injected with NNB, PNB and both beams, with the magnetic axis R_{ax_vac} positioned at 3.55 m, counter clockwise (CCW) toroidal magnetic field B_t about 2.80 T. No visible MHD mode is observed on Mirnov coils in NNB and PNB injected plasmas. Figure 4 (a) shows the time evolution of the NNB-heated plasma experiment. Here, P_{NB} and P_{ECH} represent injection powers of NB and ECH. In this discharge, P_{ECH} is around 3 MW, the acceleration voltage of the beam is around 165 keV, P_{NB} of NNB is around 2 MW, T_{e0} is around 4 keV, n_{e_avg} is around 2×10^{19} m^{-3}, and S_n is around 4×10^{14} n/s. Note that the heating power of NNB and plasma parameters are almost constant in this time period t of 5.7 s to 6.5 s. Figure 4 (b) shows the line-integrated neutron emission profile at t of 5.7 s to 6.5 s. Note that the error bar is coming from the statistical error of counts. The neutron counting rate (C_n) in the central cord (the distance between plasma axis and VNC sight line normalized by plasma minor radius r_{min}/a of 0.13) reaches 10^4 cps, whereas C_n of in the edge cord (r_{min}/a of 1.1) is 1.6×10^3 cps. Note that the very edge central cord (r_{min}/a of 1.18) is for the evaluation of the effect of scattered neutron, the C_n of 10^3 cps is sufficiently low as expected from evaluation with three dimensional Monte Carlo neutronics code [31]. In the NNB-heated plasma, the line-integrated neutron emission profile has the monotonically decreasing profile with r_{min}/a. The profile is consistent with that expected by the beam-ion-density shown in Fig 3 (a). Figure 5 (a) shows the time evolution of the PNB-heated plasma experiment. In this discharge, no ECH heating is applied, the acceleration voltage of the beam is around 70 keV, P_{NB} of PNB is around 10 MW, T_{e0} is around 2 keV, n_{e_avg} is around 2×10^{19} m^{-3}, and S_n is around 4×10^{14} n/s. Note that the S_n of this discharge is almost the same as Fig.4 (a). Figure 5 (b) shows the line-integrated neutron emission profile at t of 7.5 s to 8.5 s. Unlike NNB-heated plasma, C_n in central cords (r_{min}/a of 0.13 to 0.43) becomes relatively flat and there is steep gradient r_{min}/a of around 0.5. The profile is consistent with that expected by the beam-ion-density shown in Fig 3 (b). Figure 6 (a) shows the time evolution of both NNB- and PNB-heated plasma experiment. In this

discharge, P_{ECH} is around 2 MW, the acceleration voltage and P_{NB} of the NNB are around 150 keV and 4 MW, respectively, the acceleration voltage and P_{NB} of the PNB are around 70 keV and 10 MW, respectively, T_{e0} is around 4 keV, n_{e_avg} is around 2×10^{19} m^{-3}, and S_n is around 1×10^{15} n/s. Figure 6 (b) shows the line-integrated neutron emission profile at t of 3.5 s to 4.5 s. C_n is highest among those three discharges, which is consistent with S_n value. The line-integrated neutron emission profile is basically the monotonically decreasing profile with r_{min}/a but has relatively steep gradient at r_{min}/a of 0.5 as expected from the profiles shown in Figs.4 (b) and 5 (b).

Line-integrated neutron emission profile is measured in EIC discharges with NNB and PNB heating where NNBs inject hydrogen (H) beams and PNBs inject D beams. Hence, neutron emission is mainly due to reactions of helically-trapped beam ions and plasmas. Figure 7 shows the time evolution of EIC discharge. The magnetic configuration of this discharge is R_{ax_vac} and B_t of 3.62 m and 2.83 T, respectively. The direction of the toroidal magnetic field is CCW from the overhead view. In this discharge, there is no ECH injection, the acceleration voltage and P_{NB} of NNB are around 180 keV and 12 MW, respectively, the acceleration voltage and P_{NB} of the PNB are around 70 keV and up to 15 MW, respectively, T_{e0} is around 3 keV, n_{e_avg} is suddenly increased from $0.7\times10^{19}m^{-3}$ to $2\times10^{19}m^{-3}$ at t of around 4.6 s due to the carbon pellet injection, and W_p of the plasma is also increased from 550 kJ to 950 kJ according to the density increase. The beam modulation of PNB is for measuring the ion temperature by the charge exchange recombination spectroscopy. The strong magnetic fluctuation of EIC is observed in b_θ concurrent with intensive PNB injections. The typical b_θ of EIC is around 8×10^{-4} T at the Mirnov coil position. Time evolution of S_n shows that the decay of S_n with EIC burst (t of 4.77 s, 4.96 s, and 5.08 s) becomes significantly faster than that of without EIC burst (t of 4.67 s, 4.88 s, and 5.17 s). The maximum C_n in this discharge is around 80 counts per 10 ms in central cords (r_{min}/a of ~0.02, 0.18, and 0.35). Decreases of C_n due to EIC bursts are observed in the central cords (r_{min}/a of ~0.02, ~0.18, ~0.35, and ~0.49), whereas there is almost no change in the others. Figure 8 (a) shows the drop rate of S_n due to an EIC burst (ΔS_n) and that of C_n (ΔC_n) as the function of maximum b_θ of the EIC burst (b_{θ_EIC}). It is found that ΔS_n increase with the increase of b_{θ_EIC} and the ΔS_n reaches 50 %. The dependence of ΔC_n on b_{θ_EIC} and the value of ΔC_n are almost the same as ΔS_n. Note that in the low b_{θ_EIC} region, ΔC_n cannot be evaluated because there is no clear decrement of C_n due to low C_n. Line-integrated neutron profiles just before and after the EIC excitation are compared in Figure 8 (b). The figure indicates that the neutron counts in central cords (r_{min}/a of < 0.5) decrease by around 50 % due to the EIC burst whereas the counts in the other central cord are unchanged. The large decrease of neutron counts in central cords

indicates that substantial helically-trapped beam ions are lost due to EIC.

Line-integrated neutron profiles are measured in the EIC discharge with D-NNB- and D-PNB-heating in R_{ax_vac} of 3.62 m and B_t of 2.83 T (Fig. 9). The direction of the toroidal magnetic field is CCW from the top view. Here P_{NB} of NNB and PNB are almost constant in this time period t of 3.5 s to 4.5 s. In this discharge, T_{e0} is around 5 keV, n_{e_avg} is around 0.8×10^{19}m^{-3}, and W_p of plasma is around 600 kJ. Time evolution of S_n shows the decay of S_n synchronized with EIC bursts (t of 3.83 s, 4.02 s, 4.26 s and 4.45 s). Time evolution of C_n shows that maximum C_n in this discharge is around 200 count per 10 ms in central cord (r_{min}/a of ~0.03). Decreases of C_n due to EIC bursts are observed in central cords (r_{min}/a of ~0.03, ~0.12 and ~0.28) whereas there is almost no change in the others. Figure 10 (a) shows the ΔS_n and ΔC_n as a function of b_{θ_EIC}. As observed in H-NNB- and D-PNB-heated discharges ΔS_n and ΔC_n increase with b_{θ_EIC} and ΔC_n has almost the same value with ΔS_n. However, ΔS_n and ΔC_n reach almost one-half compared with the results shown in Fig. 8(b) although b_{θ_EIC} is comparable. The transport of helically-trapped ions is thought to be the same as Fig. 8. Therefore, the decreases of the drop rate are expected to be due to the behavior of passing beam ions. Line-integrated neutron profiles just before and after the EIC excitation are compared in Fig. 10(b). Neutron counts in core cords ($r_{min}/a < 0.3$) decreases by around 25 % and the steep gradient existing in r_{min}/a of around 0.3 becomes broader due to EIC. The counts in middle to edge codes ($r_{min}/a > 0.3$) are unchanged. The decrease of neutron counts in core cords is due to the loss of helically-trapped beam ion as observed in Figs. 7 and 8. Because the density of passing beam ions is nearly symmetrical with the poloidal angle, no or small change of neutron counts in the edge cords suggests that the effect of EIC on passing beam ions is not significant even around the EIC peak (r_{min}/a of around 0.85).

4. Summary

Research on the effect of EIC on beam ion confinement is performed in LHD D operations by means of NFM and VNC. The line-integrated neutron emission profiles are measured in MHD-quiet discharges with three cases: PNB injection, NNB injection, and NNB and PNB injections. The profile obtained in the experiment is consistent with that expected by the beam ion density calculated by orbit following models. In EIC discharge, significant decrease of S_n and C_n is observed synchronized with EIC bursts. It is found that both ΔS_n and ΔC_n increase with b_{θ_EIC}. It is also found that in H-NNB and D-PNB heated plasma, ΔS_n and ΔC_n in central cords are up to 50 %, whereas D-NNB and D-PNB heated plasma, ΔS_n and ΔC_n in central cords are up to 25 %. The line-integrated neutron profiles before and after EIC show that the neutron counts in central cords are

significantly dropped whereas the neutron counts in edge cords are almost unchanged. Hence, the experimental results suggest that the effect of EIC on helically-trapped beam ion is significant, however, the effect on passing beam ions due to EIC is not significant.

Acknowledgments
This work is supported partly by LHD project budgets (ULGG801, ULHH003, and ULHH034).

References
[1] Fasoli A. *et al* 2007 Nucl. Fusion **47** S264.
[2] Jarvis O. N. 1994 Plasma Phys. Control. Fusion **36** 209.
[3] Goeler S. von, Roquemore A. L., Johnson L. C., Bitter M., Diesso M., Fredrickson E., Long D., and Stracha J. 1996 Rev. Sci. Instum. **67** 473.
[4] Roquemore A. L., Bitter M., Johnson L. C., and Goeler S. von 1997 Rev. Sci. Instum. **68** 544.
[5] Perez von Thun C. *et al* 2012 Nucl. Fusion **52** 094010.
[6] Kiptily V. G. *et al* 2009 Nucl. Fusion **49** 065030.
[7] Ishikawa M. *et al* 2005 Nucl. Fusion **45** 2005.
[8] Takechi M. *et al* 2005 Phys. Plasmas **12** 082509.
[9] Beralot L. *et al* 2012 JINST **7** C04012.
[10] Chen L. 1994 Phys. Plasmas **1** 1519.
[11] Strachan J.D. et al 1985 Nucl. Fusion 25 863
[12] Zweben S.J. et al 1994 Phys. Plasmas 1 1469
[13] Heidbrink W.W. and Sager G. 1990 Nucl. Fusion 30 1015
[14] Fredrickson E.D., Bell R.E., Darrow D.S., Fu G.Y. and Gorelenkov N.N. 2006 Phys. Plasmas **13** 056109
[15] Heidbrink W.W., Kaita R., Takahashi H., Gammel G., Hammet G.W. and Kaye S. 1987 Phys. Fluids **30** 1839.
[16] Heidbrink W.W., Doung H.H., Manson J., Wilfrid E., Oberman C. and Strait E.J. 1993 Phys. Fluids B **5** 2176.
[17] Toi. K., Isobe M., Osakabe M., Ogawa K., Spong D.A., Todo Y., and LHD Experiment Group 2010 Contrib. Plasma Phys. **50** 493.
[18] Du X. D. *et al* 2015 Nucl. Fusion **56** 016002.
[19] Osakabe M. *et al* 2017 Fusion Sci. Technol. **72** 199.
[20] Isobe M. *et al* 2014 Rev. Sci. Instrum **85** 11E114.
[21] Ogawa K., Isobe M., Takada E., Uchida Y., Ochiai K., Tomita H., Uritani A., Kobuchi

T., and Takeiri Y. 2014 Rev. Sci. Instrum **85** 11E110.
[22] Peterson B. J. *et al* 2010 Fusion Sci. Technol. **58** 412.
[23] Yamada I., Narihara K., Funaba H., Minami T., Hayashi H., Kohmoto T., and LHD Experiment Group 2010 Fusion Sci. Technol. **58** 345.
[24] Sakakibara S., Yamada H., and LHD Experiment Group 2010 Fusion Sci. Technol. **58** 471.
[25] Spong D.A. 2011 Phys. Plasmas **18** 056109.
[26] Hirshman S. P. and Betancourt O. 1991 J. Comput. Phys. **96** 99.
[27] Seki R. *et al* 2013 Nucl. Fusion **53** 063016.
[28] Seki R., Matsumoto Y., Suzuki Y., Watanabe K., Hamamatsu K., and Itagaki M., 2010 Plasma Fusion Res. **5** 014.
[29] Seki R. *et al* 2010 Plasma Fusion Res. **5** 014.
[30] Murakami S., Nakajima N., and Okamoto M. 1995 Trans. Fusion Technol. **27** 256.
[31] Nishitani T., Ogawa K., and Isobe M. 2017 Fusion Eng. Des. **123** 1020.

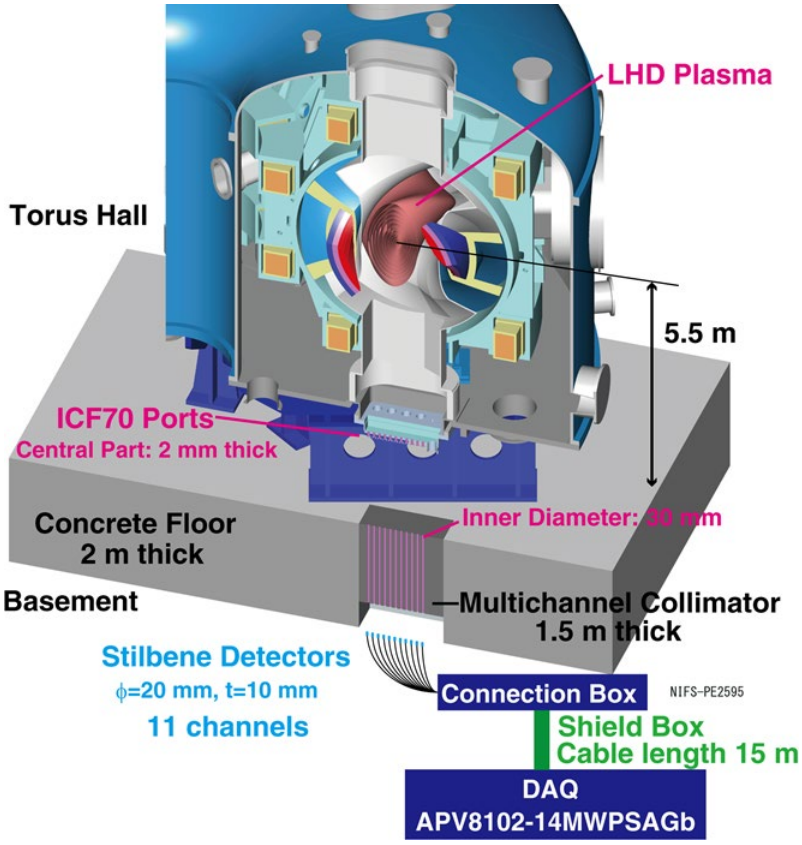

Fig.1 Vertical neutron camera installed in LHD.

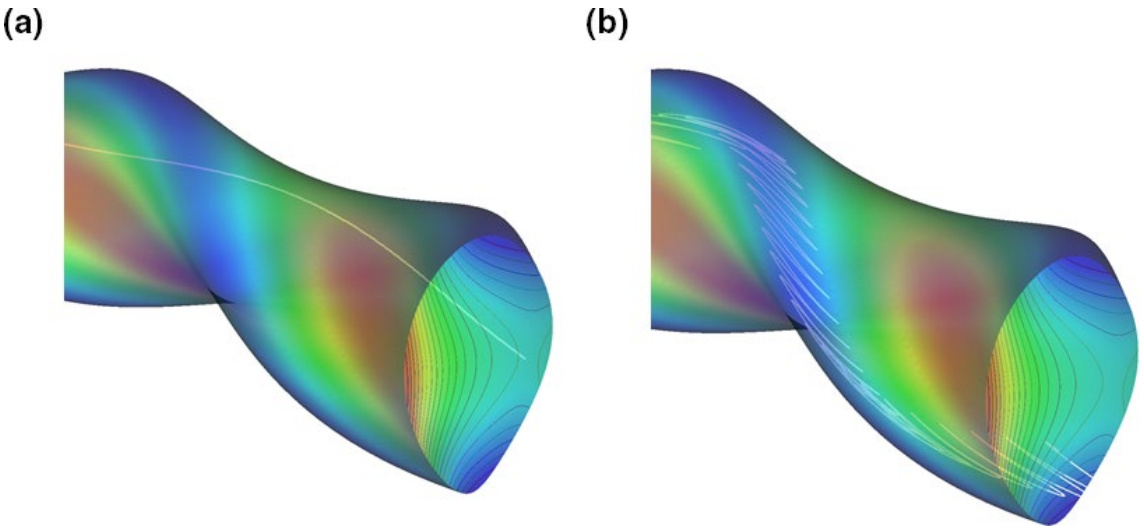

Fig.2 (a) Typical guiding center orbit of a co-going energetic ion having the energy and pitch angle of 180 keV and 25 degrees. (b) Typical orbit of a helically-trapped energetic ion having the energy and pitch angle of 80 keV and 85 degrees. The color image shows the magnetic field strength.

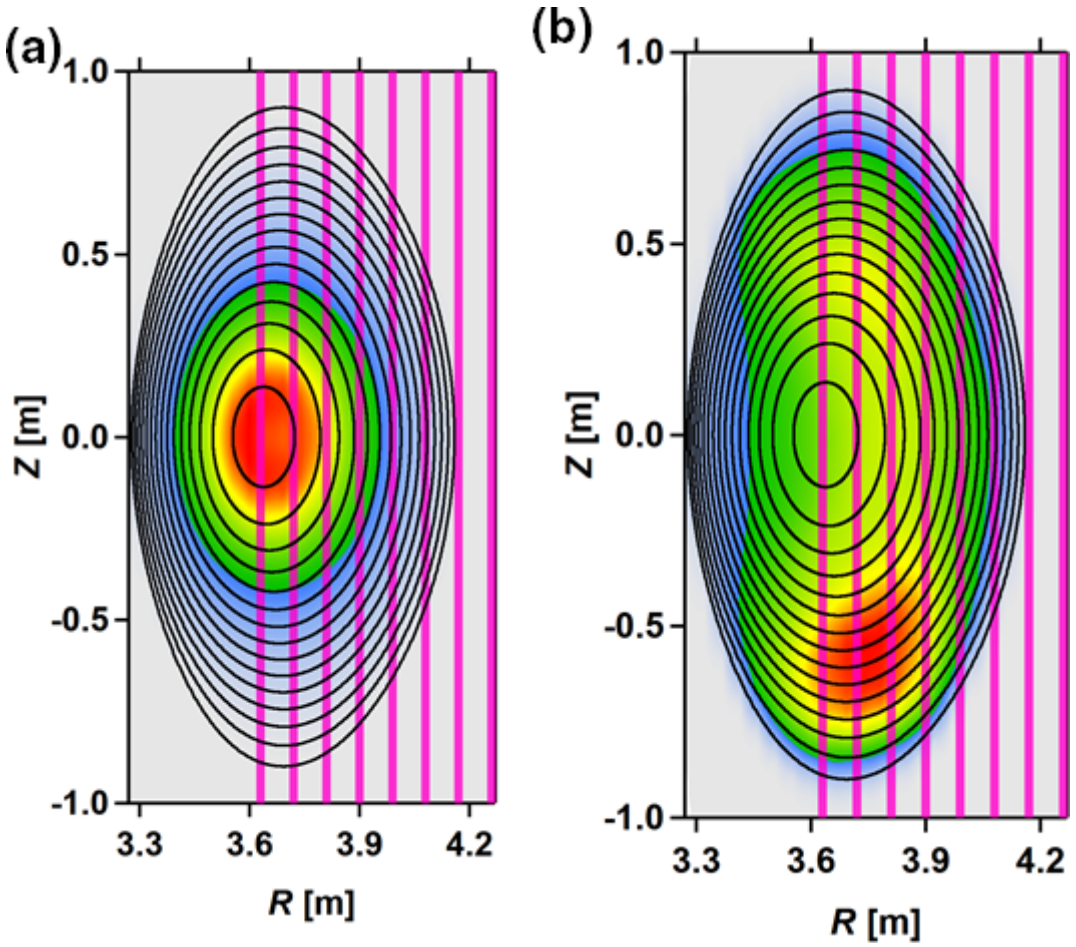

Fig. 3 Typical density profiles of (a) co-going energetic ions injected by NNB and (b) helically-trapped ions injected by PNB.

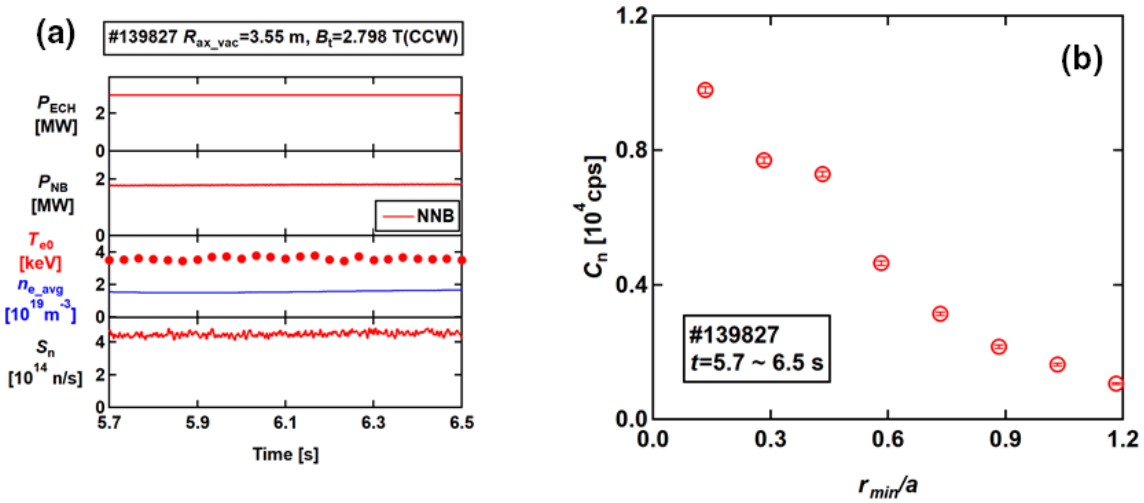

Fig.4 (a) Time evolution of MHD-quiet D-NNB-heated discharge. (b) Line-integrated neutron emission profile measured by the VNC. The neutron counting rate monotonically decreases with r_{min}/a.

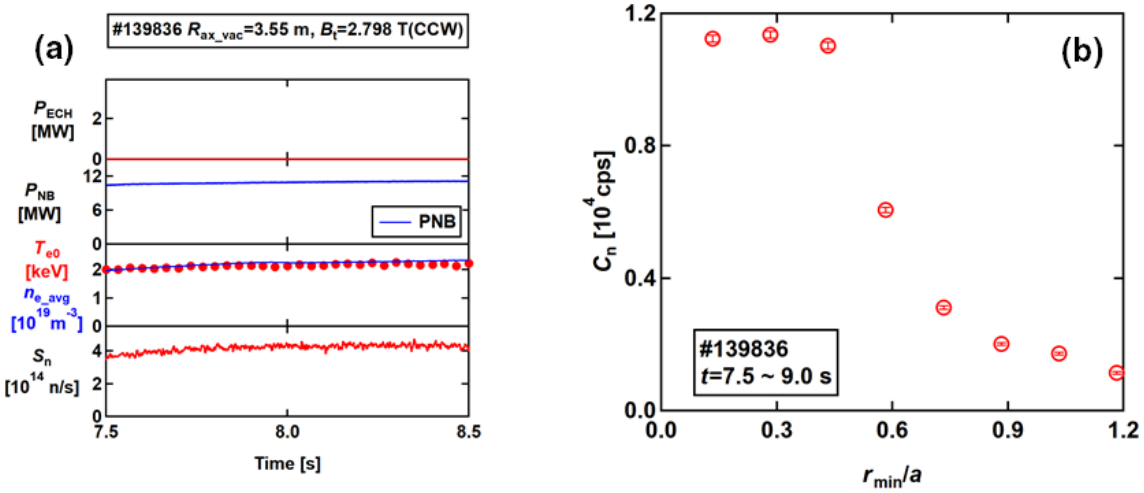

Fig.5 (a) Time evolution of MHD-quiet D-PNB-heated discharge. (b) Line-integrated neutron emission profile measured by the VNC. The neutron counting rate has a flat profile in central cords (r_{min}/a <0.45) and has steep gradient around r_{min}/a of 0.5.

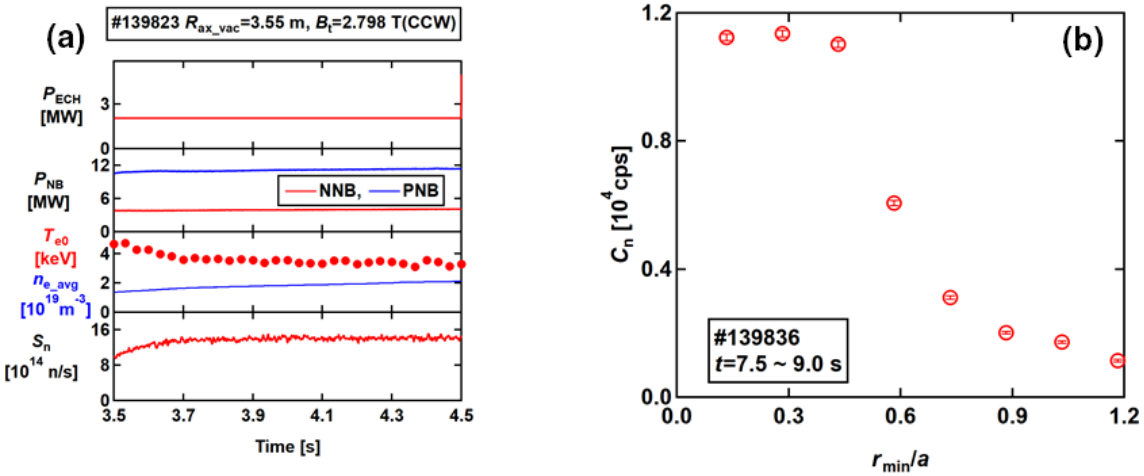

Fig.6 (a) Time evolution of MHD quiet D-NNB and D-PNB heated discharge. (b) Line-integrated neutron emission profile measured by the VNC. The neutron counting rate monotonically decreases with r_{min}/a and has a gradient around r_{min}/a of 0.5.

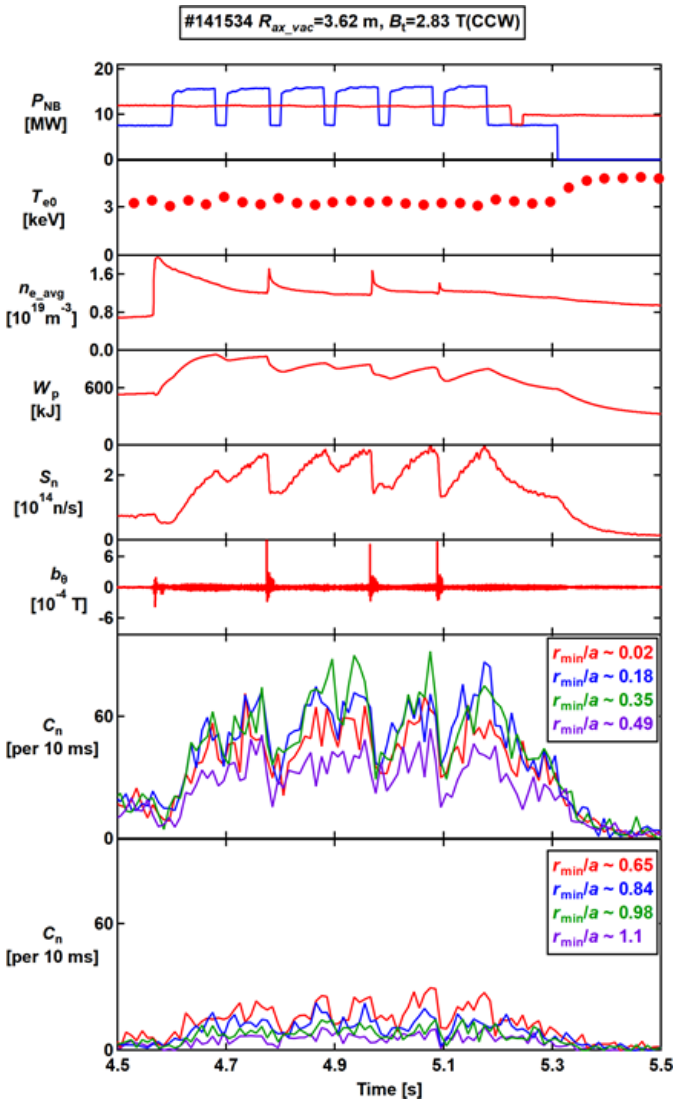

Fig. 7 Time evolution of EIC discharge with H-NNB and D-PNB heating. Decreases of C_n with EIC bursts are clearly observed in central cord ($r_{min}/a < 0.5$).

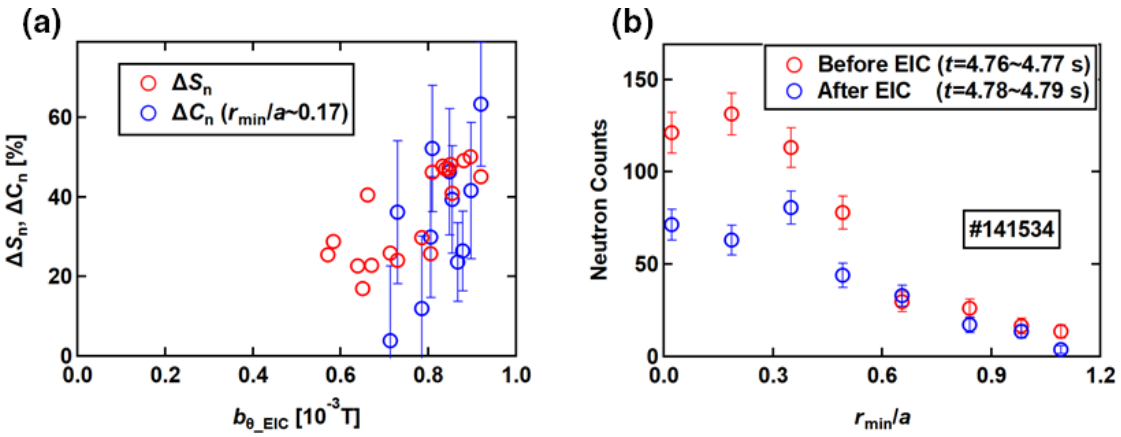

Fig. 8 (a) Dependence of ΔS_n and ΔC_n on b_{θ_EIC}. Both ΔS_n and ΔC_n decrease with b_{θ_EIC}. (b) Line-integrated neutron emission profile just before and after EIC burst.

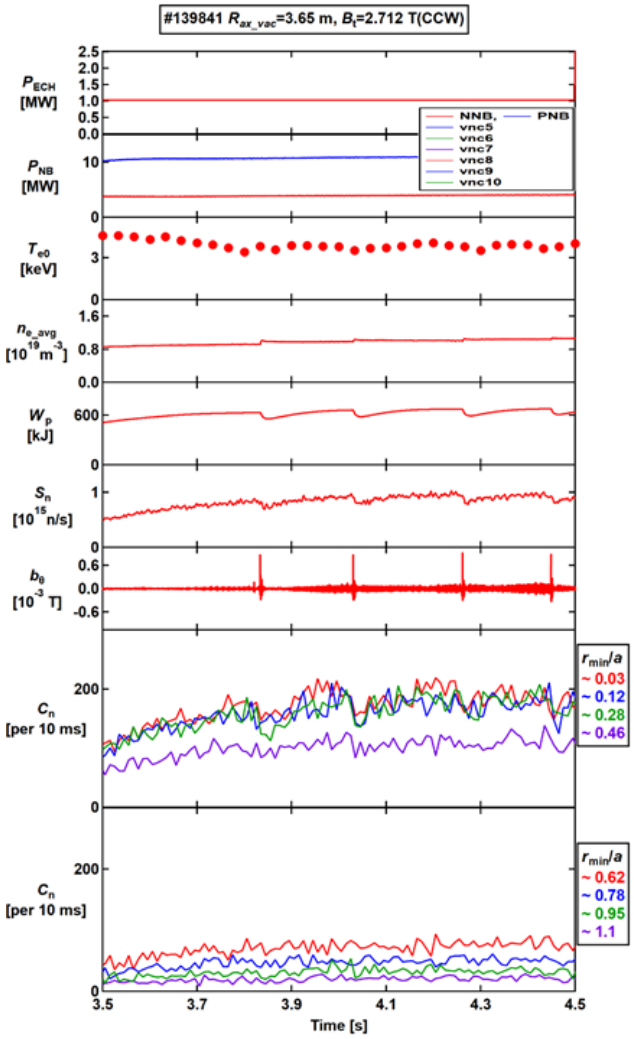

Fig. 9 Time evolution of EIC discharge with D-NNB and D-PNB heating. Decreases of C_n with EIC bursts are observed in central cords ($r_{min}/a < 0.3$)

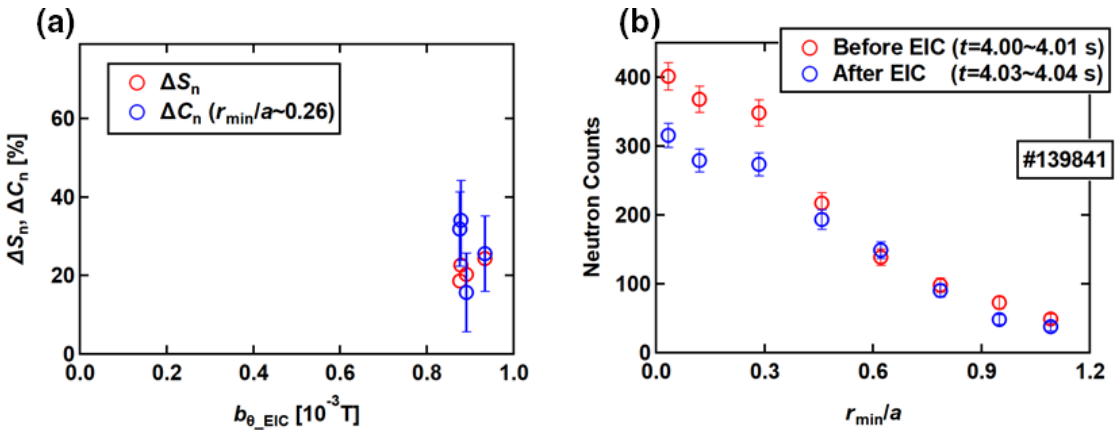

Fig.10 (a) Dependence of ΔS_n and ΔC_n on b_{θ_EIC}. Both ΔS_n and ΔC_n decrease with b_{θ_EIC}. (b) Line-integrated neutron emission profile just before and after EIC burst.